

SUN-TO-EARTH CHARACTERISTICS OF THE 2012 JULY 12 CORONAL MASS EJECTION AND ASSOCIATED GEO-EFFECTIVENESS

HUIDONG HU^{1,2}, YING D. LIU^{1,2}, RUI WANG¹, CHRISTIAN MÖSTL^{3,4}, AND ZHONGWEI YANG¹

¹State Key Laboratory of Space Weather, National Space Science Center, Chinese Academy of Sciences, Beijing 100190, China;
liuxying@spaceweather.ac.cn

²University of Chinese Academy of Sciences, No.19A Yuquan Road, Beijing 100049, China

³Space Research Institute, Austrian Academy of Sciences, A-8042 Graz, Austria

⁴IGAM-Kanzelhöhe Observatory, Institute of Physics, University of Graz, A-8010 Graz, Austria

ABSTRACT

We analyze multi-spacecraft observations associated with the 2012 July 12 Coronal Mass Ejection (CME), covering the source region on the Sun from *SDO*, stereoscopic imaging observations from *STEREO*, magnetic field characteristics at *MESSENGER*, and type II radio burst and *in situ* measurements from *Wind*. A triangulation method based on *STEREO* stereoscopic observations is employed to determine the kinematics of the CME, and the outcome is compared with the result derived from the type II radio burst with a solar wind electron density model. A Grad-Shafranov technique is applied to *Wind in situ* data to reconstruct the flux-rope structure and compare it with the observation of the solar source region, which helps understand the geo-effectiveness associated with the CME structure. Conclusions are as follows: (1) the CME undergoes an impulsive acceleration, a rapid deceleration before reaching *MESSENGER*, and then a gradual deceleration out to 1 AU, which should be noticed in CME kinematics models; (2) the type II radio burst was probably produced from a high-density interaction region between the CME-driven shock and a nearby streamer or from the shock flank with lower heights, which implies uncertainties in the determination of CME kinematics using solely type II radio bursts; (3) the flux-rope orientation and chirality deduced from *in situ* reconstruction at *Wind* agree with those obtained from solar source observations; (4) the prolonged southward magnetic field near the Earth is mainly from the axial component of the largely southward inclined flux rope, which indicates the importance of predicting both the flux-rope orientation and magnetic field components in geomagnetic activity forecasting.

Keywords: shock waves — solar-terrestrial relations — solar wind — Sun: coronal mass ejections (CMEs) — Sun: radio radiation

1. INTRODUCTION

Coronal Mass Ejections (CMEs) are massive expulsions of magnetized plasma from the solar atmosphere. They are called interplanetary CMEs (ICMEs) after traveling into interplanetary space, which are a significant class of triggers of geo-effectiveness. Understanding CME propagation, associated radio bursts, and plasma and magnetic field characteristics in the inner heliosphere is of critical importance for space weather forecasting. Combination of comprehensive remote-sensing and *in situ* observations is key to these investigations.

Previous studies of CME interplanetary propagation categorize CMEs into fast and slow ones by comparing their speed with the average solar wind speed. Slow CMEs experience an acceleration while fast ones decelerate when interacting with the ambient solar wind (Sheeley et al. 1999; Gopalswamy et al. 2000). Combining coronagraph images with *in situ* measurements, Lindsay et al. (1999); Gopalswamy et al. (2001a) obtain empirical models describing propagation of CMEs out to 1 AU. Gopalswamy et al. (2001a) find that a fast CME undergoes a deceleration out to 0.76 AU before moving at a constant speed. These studies are based on coronagraph images with a field of view (FOV) only out to 30 R_☉ and lack direct measurements between the Sun and Earth. The *Solar Terrestrial Relations Observatory* (*STEREO*; Kaiser et al. 2008) with wide-angle imaging sensors is capable of tracking CMEs from the Sun out to the Earth and even beyond. *STEREO* consists of two spacecraft, one leading the Earth (*STEREO A*) and the other trailing behind (*STEREO B*), which separate by approximately 44 to 45 degrees from each other every year.

An identical imaging suite, the Sun-Earth Connection Coronal and Heliospheric Investigation (SECCHI; Howard et al. 2008), is aboard each spacecraft, which consists of an extreme ultraviolet imager (EUVI), two coronagraphs (COR1 and COR2) and two heliospheric imagers (HI1 and HI2). A radio and plasma wave investigation instrument (SWAVES; Bougeret et al. 2008) is also mounted, which can detect type II radio bursts associated with CME-driven shocks. Based on coordinated *STEREO* stereoscopic images, a geometric triangulation technique has been developed to track CMEs with no free parameters (Liu et al. 2010a,b). With the triangulation method, it is revealed that fast CMEs impulsively accelerate until even after the X-ray flare maximum, and then rapidly decelerate to a nearly constant speed or gradual deceleration phase (Liu et al. 2013), while slow CMEs experience a slow acceleration phase and then travel with a roughly constant speed around the average solar wind level (Liu et al. 2016). A CME could also propagate in a non-radial direction (e.g., Wang et al. 2004; Gopalswamy et al. 2009; Möstl et al. 2015; Liewer et al. 2015; Wang et al. 2015), interact with other CMEs (e.g., Lugaz et al. 2009; Gopalswamy et al. 2001b; Liu et al. 2012, 2014) or co-rotating interaction regions (e.g., Reiner et al. 1998; Rouillard et al. 2010; Liu et al. 2016), or rotate in interplanetary space (e.g., Thernisien et al. 2006; Liu et al. 2010b; Vourlidas et al. 2011), which increases difficulty to predict the CME arrival characteristics at the Earth.

The *MERcury Surface, Space ENvironment, GEOchemistry, and Ranging* (*MESSENGER*; Solomon et al. 2001) spacecraft provides a great opportunity to study CMEs inside the Earth orbit. Möstl et al. (2012) investigate the shocks, flux ropes and interactions between ejecta for a series of CMEs from 2010 July 30 to August 1 with multi-point *in situ* data from *MESSENGER*, *Venus Express*, *Wind* and *STEREO*. Radial evolution of a magnetic cloud (MC) is studied based on the data from *MESSENGER* and *STEREO B* when the two spacecraft were nearly radially aligned in 2011 November (Good et al. 2015). Using data from the *MESSENGER* magnetometer, Winslow et al. (2015) compile 61 ICMEs at Mercury between 2011 and 2014, while Good & Forsyth (2016) identify 119 ICMEs combining the data from *MESSENGER* and *Venus Express*.

Interplanetary type II radio bursts emit at the fundamental and/or harmonic of the plasma frequency, which can be applied to determine the radial distance and predict the time of arrival (ToA) of CME-driven shocks at 1 AU using a proper electron density model of the solar wind (Reiner et al. 2007; Liu et al. 2008b, 2013; Cremades et al. 2015). Using the electron density model of Leblanc et al. (1998), Liu et al. (2013) derive the radial distances of CME-driven shocks from the drift rates of type II bursts, which compare well with those acquired from the geometric triangulation technique based on *STEREO* stereoscopic white-light observations. Besides from the nose of a CME-driven shock, type II radio bursts can also be produced from the flank (Claßen & Aurass 2002; Cho et al. 2007), or a preexisting high-density solar wind structure interacting with the shock (e.g., Reiner et al. 1998, 2003; Cho et al. 2007; Feng et al. 2012). These complicate the estimate of the radial distance of a shock based on an electron density model.

Prolonged and enhanced southward magnetic fields associated with ICMEs are important triggers of geomagnetic storms, which depend on the flux-rope orientation and the axial and azimuthal magnetic field components (Yurchyshyn et al. 2001; Liu et al. 2015). A statistical study finds that the tilt angles of ICME flux ropes deduced from *in situ* force-free flux-rope models are close to the tilt angles of magnetic polarity inversion lines (PILs) in the corresponding solar source regions (Marubashi et al. 2015). A Grad-Shafranov (GS) reconstruction technique is capable of estimating the flux-rope orientation, and axial and azimuthal magnetic field components from *in situ* measurements (Hau & Sonnerup 1999; Hu & Sonnerup 2002), which has been validated by well separated multi-spacecraft measurements (Liu et al. 2008a; Möstl et al. 2009). With the GS reconstruction technique, Liu et al. (2015) find that the flux-rope axial component is a major contributor to the southward magnetic field for the 2015 June 22 geomagnetic storm while the azimuthal component plays a major role in the 2015 March 17 strong geomagnetic storm, which indicates that the flux-rope structure plays an important role in the generation and intensity of geomagnetic activity.

On 2012 July 12, a major CME erupted in NOAA AR 11520 associated with an X1.4 class flare that peaked at about 16:49 UT. The active region is the same that caused the 2012 July 23 extreme solar storm (Liu et al. 2014). A strong geomagnetic storm was triggered and reached a minimum D_{st} index of -127 nT on July 15. The magnetic field configuration and evolution in the solar source region have been investigated with remote-sensing observations and/or three-dimensional magnetohydrodynamics (3D MHD) simulations (Cheng et al. 2014; Dudík et al. 2014; Song et al. 2015; Wang et al. 2016). The CME kinematic evolution has been studied with a 3D MHD model and a semi-empirical drag model by Shen et al. (2014) and Hess & Zhang (2014), respectively. This event is also included as an illustration in statistical analyses of Möstl et al. (2014) and Winslow et al. (2015).

In this paper we present a comprehensive remote-sensing and *in situ* analysis of the 2012 July 12 CME. Despite a number of previous studies of this event, our work is unique for reasons given below: (1) a triangulation method based on stereoscopic wide-angle imaging observations is employed to determine the CME kinematics in this study, while the previous studies are limited to single-spacecraft analysis; (2) the stereoscopic imaging results are compared with multi-

point *in situ* measurements at Mercury and the Earth; (3) the frequency drift rate of the type II radio burst associated with the event is analyzed in this work, from which the results are compared with the triangulation analysis; (4) we apply the GS technique to the near-Earth *in situ* data to reconstruct the flux-rope structure, and the result is compared with the solar source observations to understand the association of the flux-rope properties with the generation of the geomagnetic storm. As far as we know, the comparison between stereoscopic wide-angle imaging observations and multi-point *in situ* measurements, which can give crucial information on CME kinematics and structure, is still lacking. The comparison of wide-angle imaging observations with long-duration interplanetary type II radio bursts can also yield important knowledge of CME kinematics as well as source regions of the type II bursts, which has not been sufficiently studied. The examination of the CME magnetic structure and its comparison with the analysis of the solar source region are key to understanding how the CME structure/solar source signature is connected with geomagnetic activity. We describe the solar source signatures in Section 2 and propagation characteristics in interplanetary space in Section 3. Section 4 examines the properties of the flux rope and the associated geo-effectiveness. These results are summarized and discussed in Section 5. This work illustrates an end-to-end study of the space weather chain from the Sun to Earth, highlighting the importance of multi-spacecraft remote-sensing and *in situ* observations in understanding the Sun-to-Earth characteristics and geo-effectiveness of CMEs.

2. SOURCE REGION SIGNATURES

The CME was launched from NOAA AR 11520 (source location S15°W01°), the same active region that spawned the 2012 July 23 extreme solar storm (Liu et al. 2014). It was associated with an X1.4 class flare that peaked around 16:49 UT on 2012 July 12. *SDO*/AIA (Lemen et al. 2012) 94 Å EUV images at three moments before the eruption are displayed in Figure 1. The hot channel marked by the dashed yellow curve is identified to be the erupted flux rope forming the CME (Cheng et al. 2014; Dudík et al. 2014; Song et al. 2015). The running difference image in the bottom panel clearly indicates the expansion of the flux rope as reported by Dudík et al. (2014). The PIL near the central meridian is approximately from the northwest to the southeast according to the contours from a *SDO*/HMI (Schou et al. 2012) line-of-sight magnetogram. The axial magnetic fields of the flux rope indicated by the hot channel, which start from the positive polarity, are generally pointing to the southeast near the central meridian. The overlying azimuthal components should be from the right side (positive polarity) to the left side (negative polarity) in the view from the Earth. This magnetic configuration thus forms a right-handed flux rope, which is also consistent with a statistical research that the southern hemisphere tends to produce positive magnetic helicity (Pevtsov et al. 1995). We will compare the flux-rope chirality and orientation with the *in situ* reconstruction results at *Wind*.

3. PROPAGATION IN INTERPLANETARY SPACE

We derive the kinematics of the 2012 July 12 CME using a geometric triangulation technique proposed by Liu et al. (2010a,b) based on stereoscopic imaging observations from *STEREO*. The triangulation method adopts two geometric assumptions for the CME leading edge, called fixed β ($F\beta$) and harmonic mean (HM) approximations, respectively. The $F\beta$ approximation assumes that a CME is a relatively compact structure simultaneously observed by the two spacecraft when it is moving away from the Sun (Sheeley et al. 1999; Kahler & Webb 2007; Liu et al. 2010b). The HM approximation assumes that the leading edge of a CME is a sphere which is attached to the Sun and tangent to the lines of sight of the two spacecraft (Lugaz et al. 2009; Liu et al. 2010b). A self-similar expansion model expressing the same triangulation concept is developed by Davies et al. (2013), for which the $F\beta$ and HM approximations are limiting cases. The triangulation concept has proved to be useful for acquiring CME Sun-to-Earth kinematics and connecting remote sensing observations with *in situ* signatures (e.g., Liu et al. 2010a,b, 2013; Lugaz et al. 2010; Möstl et al. 2010; Harrison et al. 2012; Temmer et al. 2012; Davies et al. 2013). Detailed descriptions and discussions of the triangulation technique can be found in Liu et al. (2010b, 2013, 2016).

Figure 2 shows the trajectories of the 2012 July 12 CME obtained from the $F\beta$ and HM triangulations as well as the positions of the planets and spacecraft in the ecliptic plane on 2012 July 13. *STEREO A* was $\sim 120^\circ$ ahead of the Earth and *B* was $\sim 115^\circ$ behind. Venus was ~ 0.73 AU from the Sun and $\sim 23.5^\circ$ west of the Earth, while *MESSENGER* (Mercury) was ~ 0.47 AU from the Sun and $\sim 30.6^\circ$ east of the Earth. This is a halo CME that impacted Mercury (*MESSENGER*), the Earth (*Wind*) and possibly Venus. The maximum speed of the CME near the Sun was ~ 2046 and ~ 1817 km s $^{-1}$ estimated by the $F\beta$ and HM triangulations, respectively.

The *STEREO* spacecraft tracked the whole propagation of the CME from the Sun to Earth with white-light observations from the SECCHI instruments. Figure 3 depicts the evolution of the CME from COR2, HI1 and HI2 of *STEREO A* and *B*. COR2 has a 0.7° – 4° FOV around the Sun. HI1 has a 20° square FOV centered at 14° elongation from the center of the Sun, while HI2 has a 70° FOV centered at 53.7° . The shock ahead of the CME ejecta is visible in the

COR2 images, which was interacting with nearby streamers. By stacking the running difference intensities of COR2, HI1, and HI2 within a slit along the ecliptic plane, we obtain two time-elongation maps (J-maps, e.g., Sheeley et al. 2008; Davies et al. 2009; Liu et al. 2010a) as shown in Figure 4. The time when the CME track intersected with the Earth elongation line in the view of *STEREO B* is a little earlier than that for *STEREO A*, which indicates that the CME was propagating in a direction slightly to the east of the Sun-Earth line (see Figure 2). Due to the contamination by the Milky Way galaxy in *STEREO A* HI2 as displayed in Figure 3, the track duration from *STEREO A* is shorter than that from *STEREO B*.

The CME kinematics in the ecliptic plane derived from the triangulation method is plotted in Figure 5. The average CME directions during the whole propagation process obtained from the two approximations are $\sim 4^\circ$ and $\sim 12^\circ$ to the east of the Sun-Earth line, respectively, which are consistent with the results obtained from the single-spacecraft self-similar expansion (SSEF) and harmonic mean (HMF) fittings (Möstl et al. 2014). The angle derived from the HM triangulation is roughly twice the one from the $F\beta$ triangulation and more variational, which is also noticed in previous studies (Lugaz et al. 2010; Liu et al. 2013, 2016). The distance derived from the $F\beta$ approximation becomes larger than that from the HM approximation around $50 R_\odot$ and the speed from the $F\beta$ approximation starts to show an unphysical acceleration around $100 R_\odot$, which are also noted in previous studies (Lugaz et al. 2009; Wood et al. 2009; Liu et al. 2013) and due to the non-optimal observation geometry of the two spacecraft (i.e., observing from behind the Sun) in combination with the $F\beta$ restriction (Liu et al. 2013, 2016). The speed trends from the $F\beta$ and HM approximations below $\sim 50 R_\odot$ are similar, except that the peak speed from $F\beta$ is $\sim 200 \text{ km s}^{-1}$ larger. Both the two speed profiles show that the CME accelerates out to $\sim 20 R_\odot$ even after the X-ray flux peak time and then rapidly drops to ~ 1400 ($F\beta$) and ~ 1200 (HM) km s^{-1} at $\sim 50 R_\odot$ in about 4 hours. The speeds during the acceleration phase are consistent with that obtained from the Graduated Cylindrical Shell (GCS) model by Möstl et al. (2014), while the latter is an average from 2.5 to $15.6 R_\odot$ which is still in the acceleration phase. The $F\beta$ speed after the acceleration phase is consistent with the constant speed of 1486 km s^{-1} derived from the SSEF fitting by Möstl et al. (2014), while the HM counterpart is smaller. Ignoring the unphysical acceleration from the $F\beta$ approximation, we can see that the CME undergoes a gradual deceleration phase after the peak speed. Both the speed profiles acquired from the $F\beta$ and HM triangulations are similar to those of the three fast CMEs in Liu et al. (2013).

The radio dynamic spectra associated with the CME from *Wind* and *STEREO* are shown in Figure 6. A long-duration type II radio burst is observed only by *Wind*, which starts from the upper boundary of 16 MHz at $\sim 17:00$ UT on July 12 after the X-ray flux peak and drifts to $\sim 250 \text{ kHz}$ at $\sim 9:00$ UT on July 13. The drift rate from $\sim 300 \text{ kHz}$ becomes more gradual around $2:00$ UT on July 13. There are several solar wind electron density models (e.g., Fainberg & Stone 1971; Saito et al. 1977; Bougeret et al. 1984) that can interpret the frequency of type II radio as the distance of emission source. We choose a popular electron density model derived by Leblanc et al. (1998, referred to as the Leblanc model hereafter) that covers a range from about $1.8 R_\odot$ to 1 AU embracing the whole triangulation derived CME propagation distance. Results of three CME events from this model agree well with those from the same triangulation method as employed in this work (Liu et al. 2013). The CME leading edge distances obtained from the triangulation with the $F\beta$ and HM approximations are converted to frequencies using the Leblanc model with an electron density $n_e = 20 \text{ cm}^{-3}$ at 1 AU , and are then doubled to their harmonic frequencies and plotted over the spectra. The frequencies from both the $F\beta$ and HM triangulations underestimate the observed type II radio band in the initial phase (before $\sim 22:00$ UT on July 12) and final phase (after $\sim 4:00$ UT on July 13), which suggests that the distances of the type II radio source regions are smaller than those derived from the triangulation method during the two time ranges. Note that the electron density of 20 cm^{-3} at 1 AU is already very high compared with the average solar wind electron density at 1 AU , and it will require an even higher electron density if we assume the type II radio emission at the fundamental frequency.

Assuming that the emission is produced at the second harmonic frequency, we derive the shock distance from the type II radio burst using the Leblanc model. The distances obtained from the electron density of $n_e = 6.5$ and $n_e = 20 \text{ cm}^{-3}$ at 1 AU are plotted in the middle panel of Figure 5. The uncertainties are obtained from the width of the type II radio band shown in Figure 6. The distance corresponding to $n_e = 6.5 \text{ cm}^{-3}$ at 1 AU is much smaller compared with the distance derived from the HM triangulation. This indicates that the electron density inferred from the radio frequency is much higher than that from the Leblanc model with $n_e = 6.5 \text{ cm}^{-3}$ at 1 AU . The more gradual increase of the distance from ~ 40 to $\sim 50 R_\odot$ suggests that the frequency drift during that time period is slower. In order to match the triangulation results, a larger electron density $n_e = 20 \text{ cm}^{-3}$ is used, from which the distance is roughly consistent with the triangulation results between $22:00$ UT on July 12 and $4:00$ UT on July 13 but is still smaller than the triangulation results outside the time range. These results imply that the type II radio burst was probably produced from the shock flank with lower heights or a high-density streamer interacting with the shock. We see more

than one streamers interacting with the shock in Figure 3, but we cannot determine which interaction produced the type II radio burst.

Figure 7 shows the solar wind magnetic field measurements by the *MESSENGER* Magnetometer (Anderson et al. 2007). *MESSENGER* was orbiting Mercury approximately in the Y-Z plane of the Mercury Solar Orbital frame with a period of 8 hours, the periapsis of 2795 km and the apoapsis of 12677 km (from the center of the planet). Data below 4 Mercury radii (9760 km), where the measurements are supposed to be dominated by the magnetosphere, are excluded. A shock with a sharp increase in the magnetic field strength was observed at 10:53 UT on July 13 before the apoapsis. The HM triangulation predicts an arrival time of the CME leading edge at *MESSENGER* around 09:39 UT on July 13 (see Figure 5) which is only about 1 hour earlier than observed at *MESSENGER*. We cannot estimate the flux-rope orientation and chirality since the magnetic field was dominated by the expanded Mercury magnetosphere for most of the time during the event. Note that the rapid deceleration occurred before the CME reached *MESSENGER* and thereafter the CME speed is roughly constant (see Figure 5). The CME also plausibly impacted *Venus Express*, since we see the putative end of the flux rope on July 15 through the magnetic field data from the spacecraft. However, we cannot determine the arrival time of the shock because there is a data gap during the CME arrival.

4. NEAR-EARTH PROPERTIES AND GEO-EFFECTIVENESS

The *in situ* measurements associated with the 2012 July 12 CME at *Wind* are presented in Figure 8, showing that a shock passed *Wind* at 17:43 UT on July 14. Due to the noisy backgrounds in *STEREO B* HI2 images (see Figure 3), the HM triangulation can track the CME out to $\sim 150 R_{\odot}$ (see Figure 5). We use a linear fit of the distances and assume a propagation direction of -10° near 1 AU to estimate the shock ToA at *Wind*. The fit predicts a ToA of 08:25 UT on July 14 which is about 9 hours earlier than the observed shock arrival, and a speed of $\sim 930 \text{ km s}^{-1}$ which is larger than the shock speed ($\sim 770 \text{ km s}^{-1}$) observed at *Wind*. A flux-rope-like structure with an interval from 7:38 UT on July 15 to 14:28 UT on July 16 is identified through the boundary sensitive GS reconstruction method (see the text below) in combination with the plasma and magnetic field parameters. In the flux rope, the magnetic field strength decreases smoothly, the R component increases from -20 nT to around zero, the T component rotates from negative to positive, and the N component keeps negative and increases from -18 to -9 nT . There is possibly another flux rope following the reconstructed one with a different magnetic configuration extending to $\sim 04:30$ UT on July 17 in the MC, which, however, can not be reconstructed by the GS method. Following the sudden commencement at the shock arrival, a major geomagnetic storm occurred because of the southward magnetic field, with the minimum D_{st} of -127 nT . Both the O'Brien & McPherron (2000) and Burton et al. (1975) D_{st} models underestimate the D_{st} measurements. This is possibly due to the low solar wind density within the MC. Previous studies reveal that a high density can intensify the ring current by feeding the plasma sheet of the magnetosphere (Farrugia et al. 2006; Lavraud et al. 2006). The geomagnetic storm would have been stronger if the density inside the MC were higher.

We obtain a cross section of a flux-rope-like structure as shown in Figure 9 using the GS reconstruction (Hau & Sonnerup 1999; Hu & Sonnerup 2002), which helps understand how the CME structure contributes to the geomagnetic storm activity. The magnetic fields are in a flux-rope frame where x is nearly along the spacecraft trajectory and z in the direction of the flux-rope axis. The structure is right-handed as inferred from the transverse fields along the spacecraft trajectory. The elevation angle of the flux-rope axis is about -44° and the azimuthal angle is about 232° in RTN coordinates, as determined from the single-valued behavior of the transverse pressure over the vector potential (Hu & Sonnerup 2002, see below). The elevation angle is comparable to the GCS results reported by Möstl et al. (2014) and Hess & Zhang (2014) based on coronagraph images. The orientation and chirality of the reconstructed flux rope are consistent with those derived from the solar source observations displayed in Figure 1. The maximum strength of the axial magnetic field is $\sim 30 \text{ nT}$, about two times as large as the maximum value of the azimuthal component (13 nT). Therefore, the axial magnetic field component on top of the largely southward orientation of the flux rope is the main contributor to the southward magnetic field triggering the geomagnetic storm.

The plot of the transverse pressure P_t versus the vector potential $A(x, 0)\hat{z}$ in Figure 10 indicates the reliability of the GS reconstruction result for this event. The transverse pressure P_t is a function of the vector potential $A(x, y)$ alone and expressed by $P_t = B_z^2/2\mu + p$, where B_z is the axial magnetic field and p is the thermal pressure (Hu & Sonnerup 2002). The measurements are fitted by a cubic polynomial, and an exponential tail is used for A less than -220.8 T m . The fitting residue $R_f \approx 0.04$ is relatively small, which proves that the single-valued relation between P_t and A required by the GS technique is satisfied (Hu et al. 2004). The GS reconstruction is sensitive to the chosen boundaries, which can help determine the MC interval at *Wind*.

5. SUMMARY AND DISCUSSIONS

We have performed a comprehensive analysis of the 2012 July 12 CME, covering the solar source observations by *SDO*, the stereoscopic remote-sensing observations from *STEREO*, the magnetic field signatures at *MESSENGER*, and the type II radio burst and *in situ* characteristics observed by *Wind*. A GS reconstruction is employed to understand the ICME structure and how the structure controls the geomagnetic activity. These results are summarized and discussed below, which illustrate the importance of multi-spacecraft remote-sensing and *in situ* observations for understanding the physical processes of CME propagation and space weather forecasting.

1. This study compares *STEREO* stereoscopic wide-angle imaging observations with multi-point *in situ* measurements at Mercury and the Earth, which places a strong constraint on CME Sun-to-Earth propagation. The CME kinematics determined from the triangulation technique predicts well the shock arrival time at *MESSENGER* with an error of about 1 hour in this study. A reasonable accuracy is also obtained when we compare the predicted arrival time and speed with the *in situ* measurements near the Earth. From the Sun to Earth, the CME undergoes an impulsive acceleration, a rapid deceleration, and then a gradual deceleration out to 1 AU, which agrees with the conclusions of Liu et al. (2013, 2016). We find that the rapid deceleration ceases at $\sim 50 R_{\odot}$ before the CME reached *MESSENGER* (~ 0.47 AU), which is different from the coronagraph findings in Gopalswamy et al. (2001a). Combining this case with the three events in Liu et al. (2013), we suggest that fast CMEs are likely to terminate deceleration before reaching 100 R_{\odot} from the Sun, which should be noticed in kinematics models of fast CMEs. This work once again proves the reliability of the stereoscopic triangulation technique in determining the kinematics of earthward CMEs in the inner heliosphere.
2. Our comparison between wide-angle imaging observations and the interplanetary type II radio burst indicates important clues on the source region of the type II burst. The study reveals that the consistency between the shock distance derived from the type II radio burst and the CME kinematics determined by the triangulation method requires an unusually high solar wind electron density. The type II radio burst was probably produced from a high-density region. This discrepancy and the slow increasing distance of the CME-driven shock derived from the type II radio burst can be explained by the shock interacting with nearby streamers (e.g., Reiner et al. 2003; Cho et al. 2007; Feng et al. 2012). Another possibility is that the type II radio burst was generated by the shock flank region with lower heights (Claßen & Aurass 2002; Knock et al. 2003). Because only one spacecraft detected the type II radio burst, it is not possible to determine the position of the source region by the radio triangulation method of Martínez-Oliveros et al. (2015). This result implies uncertainties in the determination of CME kinematics using type II radio bursts alone.
3. We reconstruct the ICME structure near the Earth in order to connect it with the solar source observations and to understand how the structure contributes to the geomagnetic storm. The flux-rope inclination angle and chirality at 1 AU are consistent with those inferred from the observations of the solar source. It is worth noting that, however, a flux rope may rotate in the corona and interplanetary space (Liu et al. 2010b; Vourlidis et al. 2011). The prolonged southward magnetic field near the Earth is mainly from the axial component of the largely southward inclined flux rope. The axial magnetic field component of the flux rope is about two times as large as the azimuthal component as revealed by the GS reconstruction. If the flux rope had not been inclined southward to the large angle in this event, the strength and duration of the southward magnetic field would be much smaller. Liu et al. (2015) reported an event with the azimuthal magnetic field component much larger than the axial component, which suggests that a southward orientation is not a necessity for a strong southward magnetic field. These results indicate the importance of predicting both the flux-rope orientation and magnetic field components in geomagnetic activity forecasting.

The research was supported by the Recruitment Program of Global Experts of China, NSFC under grant 41374173 and the Specialized Research Fund for State Key Laboratories of China. This study was supported by the Austrian Science Fund (FWF): [P26174-N27] and the European Union Seventh Framework Programme (FP7/2007-2013) under grant agreement No. 606692 [HELCATS]. The authors thank the referee and the editor for their efforts to improve this article. We acknowledge the use of data from *STEREO*, *MESSENGER*, *Wind*, *SDO*, and the D_{st} index from WDC in Kyoto.

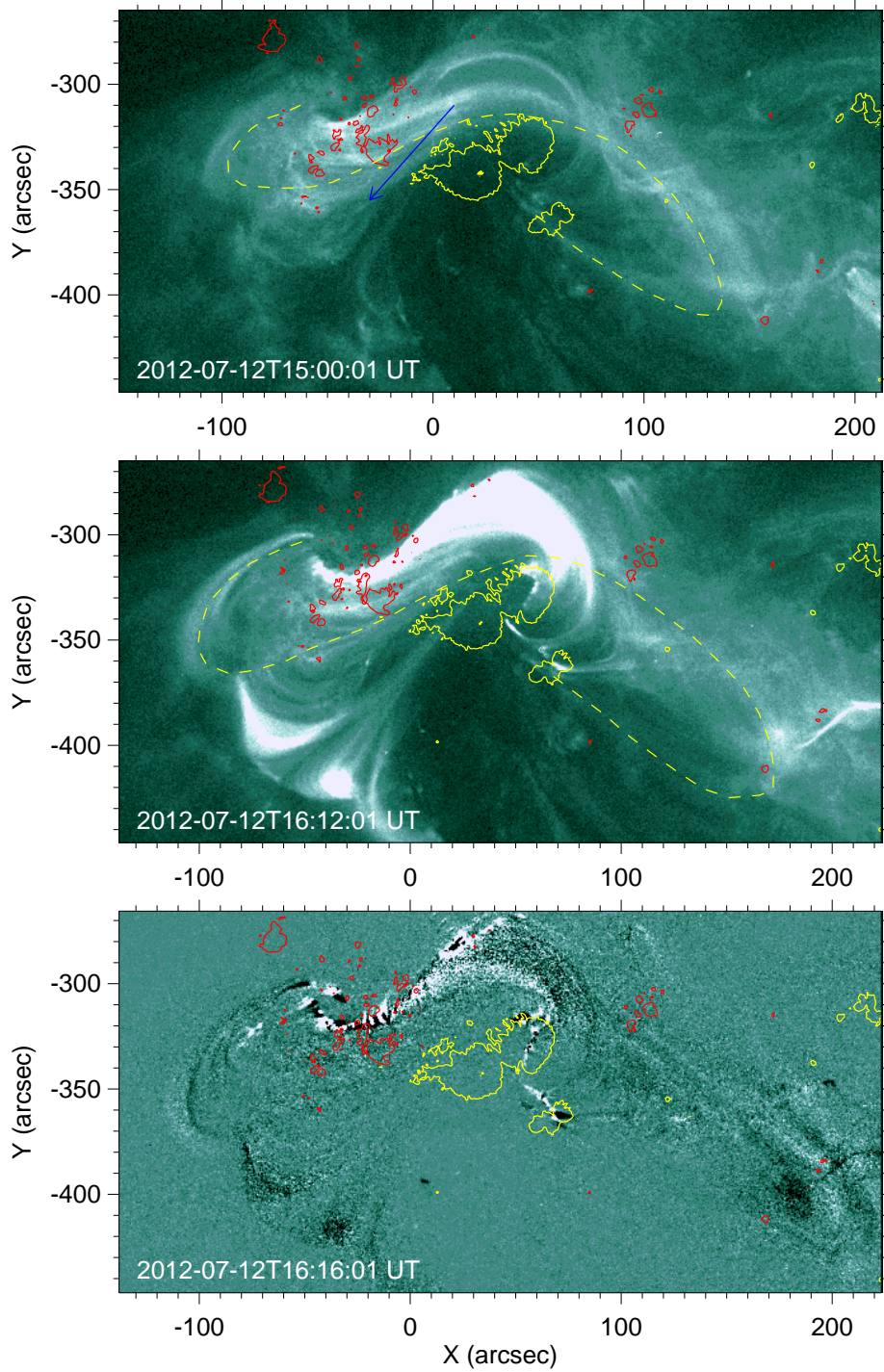


Figure 1. *SDO/AIA* 94 Å EUV images of NOAA AR 11520 before the eruption. The bottom panel shows an EUV running difference image with time delay of 1 minute. The dashed yellow curves in the top and middle panels indicate the synoptic configuration of the flux rope which produced the CME. The bright pattern in the middle panel is the low-lying flux rope that did not erupt in the event (Cheng et al. 2014). The yellow and red contours represent the areas of the magnetic field along the line of sight larger than 1000 Gauss for positive and negative polarities, respectively. The blue arrow in the top panel roughly marks the position and direction of the polarity inversion line near the central meridian.

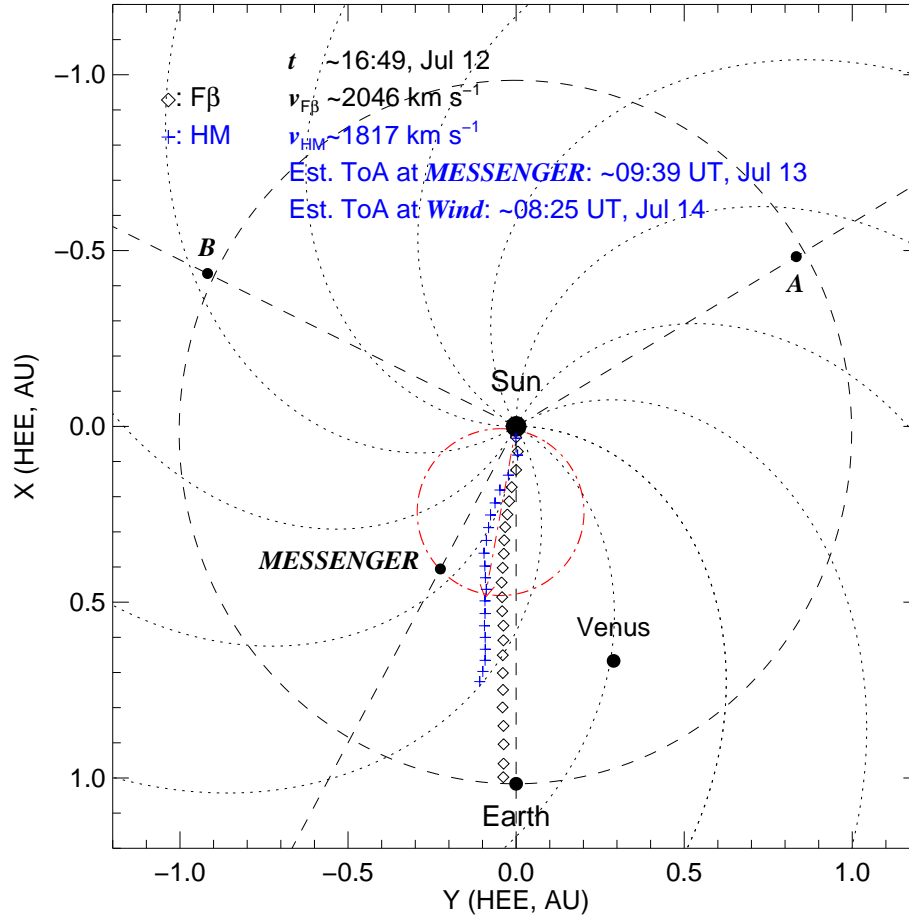


Figure 2. Positions of the spacecraft and planets in the ecliptic plane on 2012 July 13. The trajectories of the 2012 July 12 CME are obtained from triangulations with the F β (black diamond) and HM (blue cross) approximations, respectively. The red circle represents the size of the assumed spherical CME leading edge when the shock arrives at *MESSENGER*, and the red arrow indicates the direction then. The black circle marks the orbit of the Earth, and the gray dotted curves show Parker spiral magnetic fields created with a solar wind speed of 450 km s^{-1} . The estimated CME launch time on the Sun and derived peak speeds are given. The estimated arrival times of the shock at *MESSENGER* and *Wind* by the HM approximation are printed in blue.

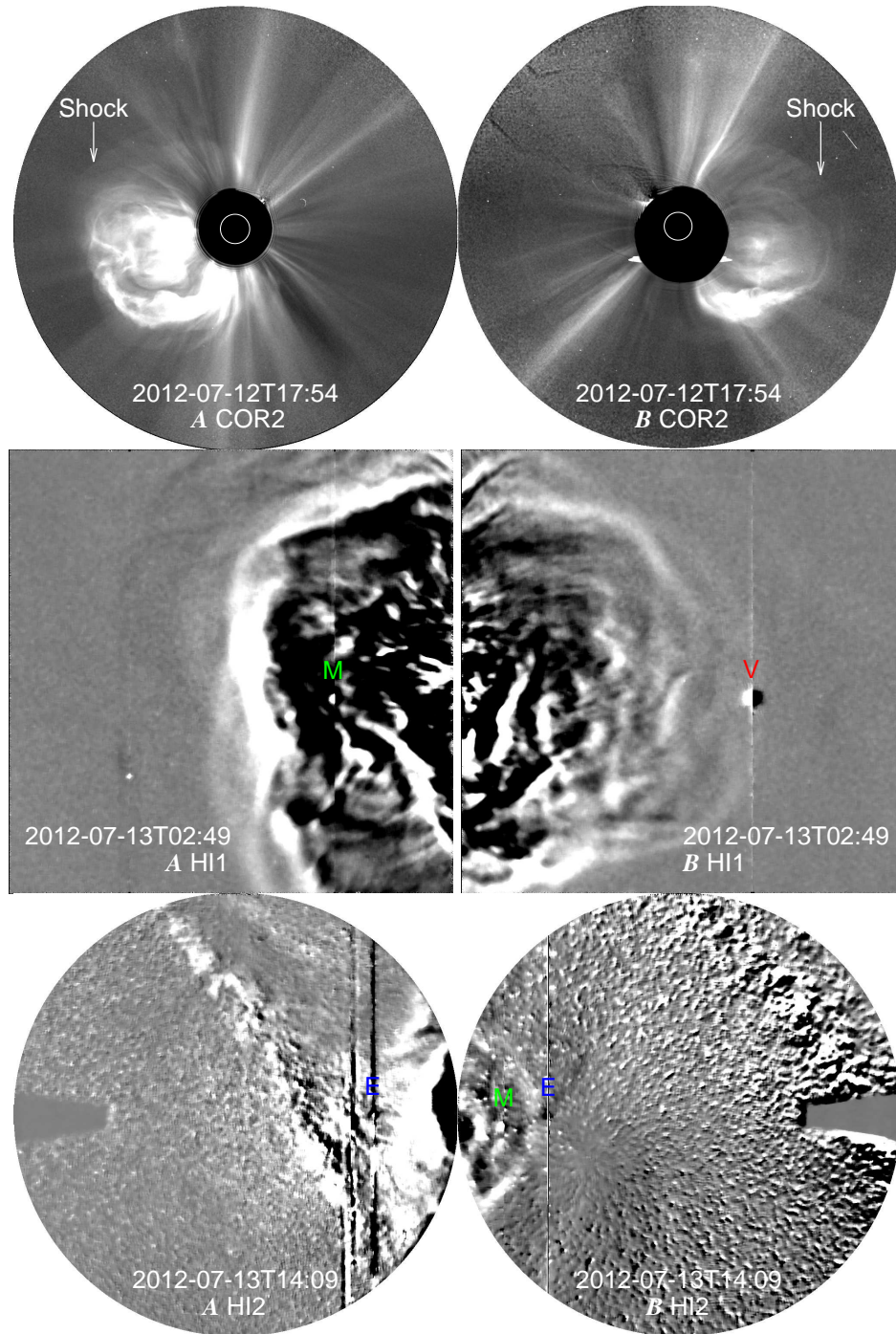


Figure 3. Evolution of the 2012 July 12 CME viewed simultaneously from *STEREO A* (left) and *B* (right). From top to bottom, the panels show the images of COR2, running difference images of HI1 and HI2, respectively. The shock driven by the CME is visible in the COR2 images. The positions of Mercury (M), Venus (V) and the Earth (E) in the fields of view are marked in corresponding HI images.

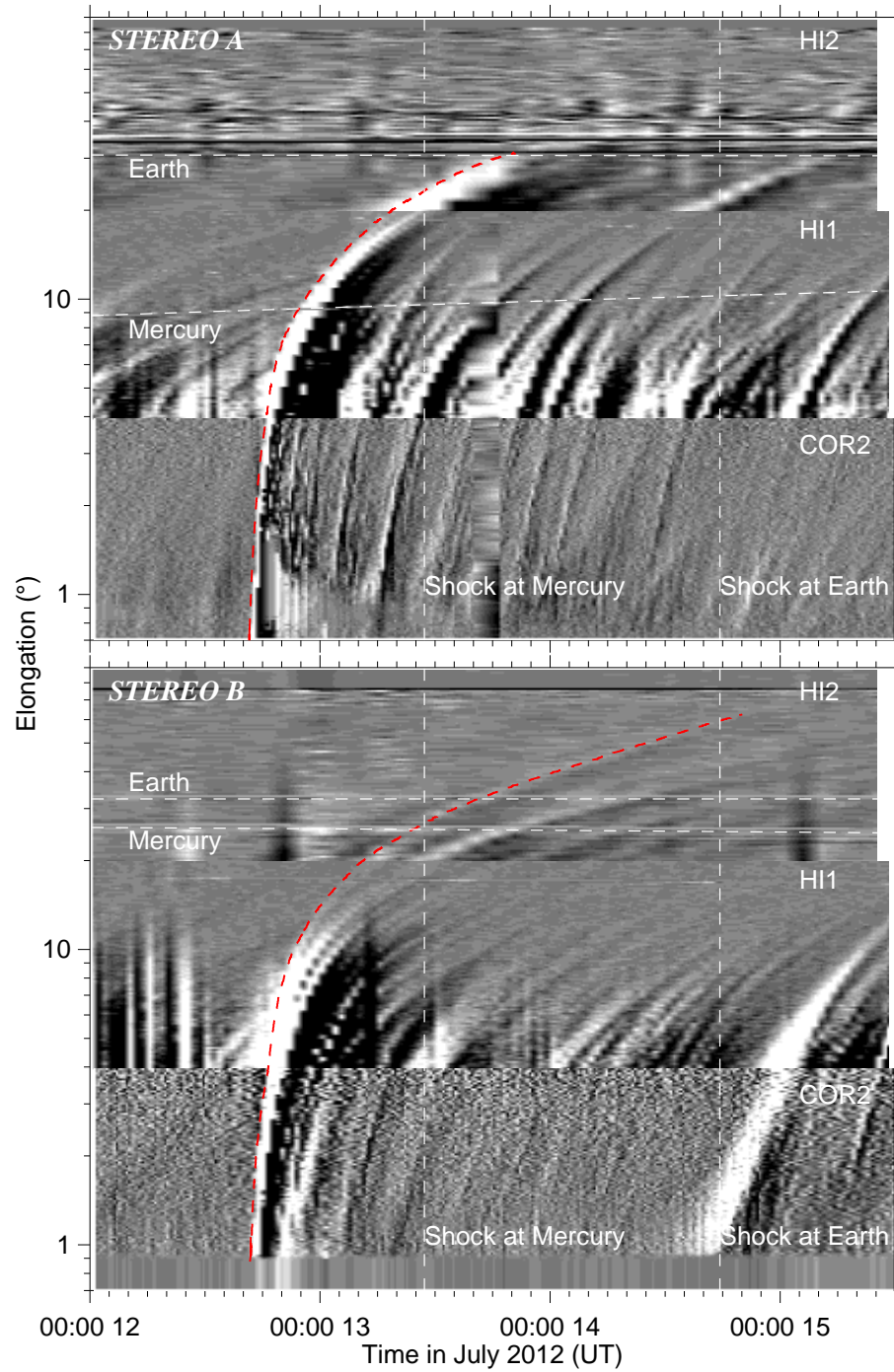


Figure 4. Time-elongation maps constructed from running difference images along the ecliptic plane. The red dashed curve indicates the CME track, along which the elongation angles are extracted. The vertical dashed lines mark the observed arrival times of the shock at Mercury and the Earth. The horizontal dashed lines denote the elongation angles of the Earth and Mercury.

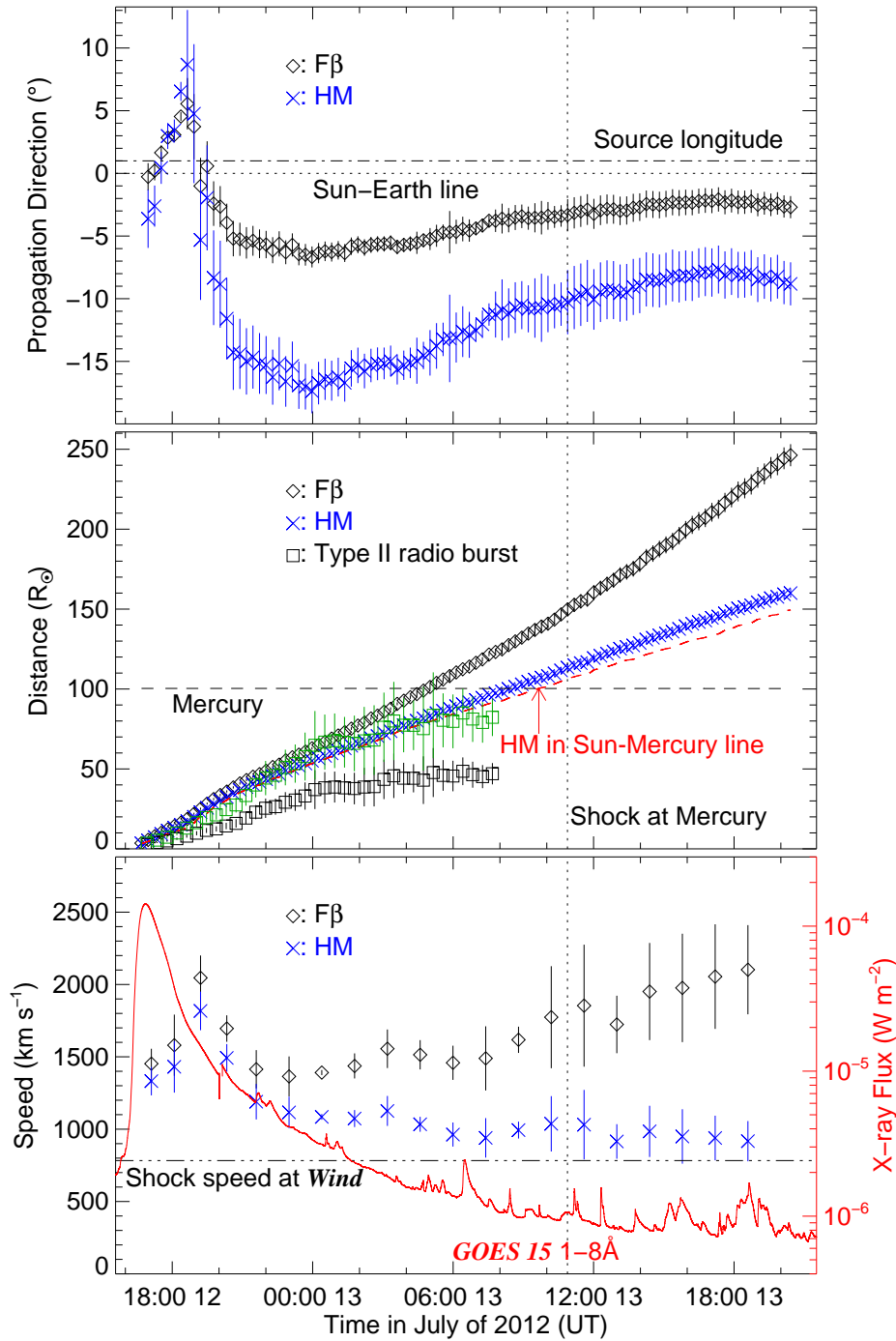


Figure 5. Propagation direction, radial distance and speed profiles of the leading edge of the 2012 July 12 CME derived from triangulations with the F β (black diamond) and HM (blue cross) approximations. The Sun-Earth line and the longitude of the CME source location on the Sun are indicated by the horizontal lines in the top panel. In the middle panel, the black squares denote the distances derived from the associated type II radio burst using the Leblanc model with an electron density of 6.5 cm^{-3} at 1 AU, while the green squares are corresponding distances obtained with an electron density of 20 cm^{-3} at 1 AU. The red dashed curve indicates the HM triangulated distance of the CME leading edge along the Sun-Mercury line, and the horizontal line in the middle panel marks the distance of Mercury. The speeds are calculated from adjacent distances using a numerical differentiation with three-point Lagrangian interpolation and are then binned to reduce the scatter. The horizontal line in the bottom panel indicates the shock speed measured at *Wind*, and the red curve is the *GOES 15 1-8Å* X-ray flux scaled by the red axis on the right. The vertical dotted line marks the arrival time of the shock at *MESSENGER*.

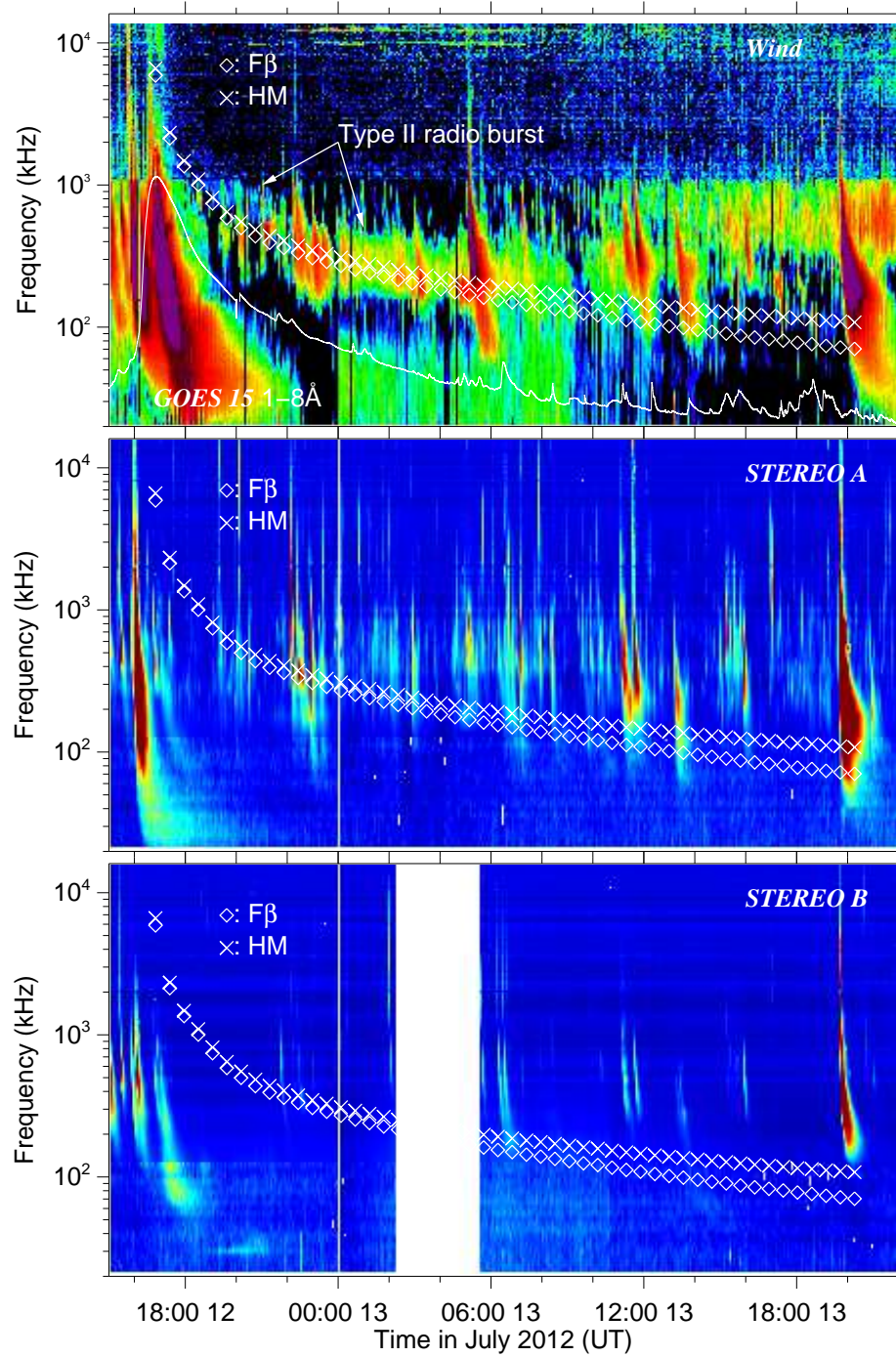


Figure 6. Radio dynamic spectra associated with the 2012 July 12 CME from *Wind*, *STEREO A* and *B*. The CME leading edge distances derived from triangulation with the $F\beta$ (diamond) and HM (cross) approximations are converted to frequencies using the Leblanc model with $n_e = 20 \text{ cm}^{-3}$ at 1 AU, and then plotted over the dynamic spectra. *GOES* X-ray flux is also overlapped in the *Wind* plot scaled in arbitrary units. The white area in the bottom panel indicates the data gap.

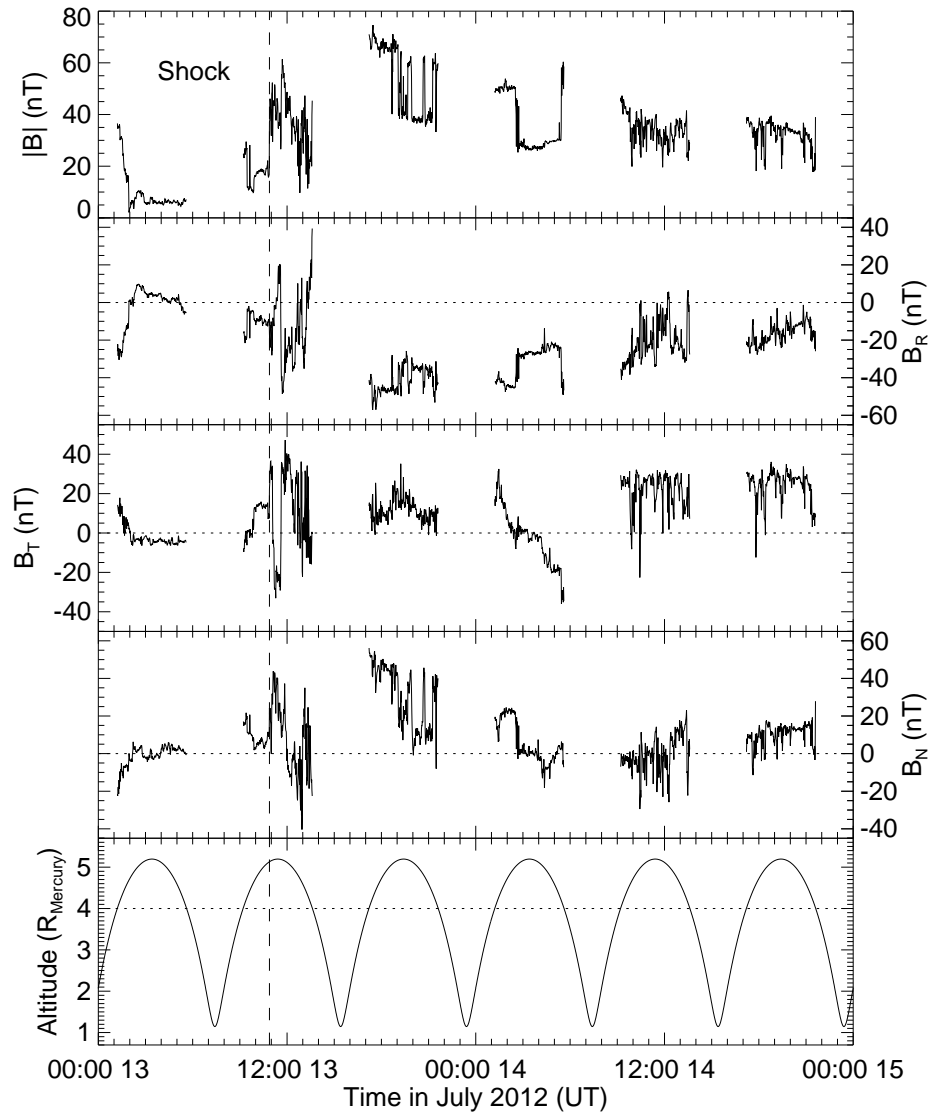


Figure 7. Magnetic field strength and components at *MESSENGER*. Also shown is the orbital altitude from the center of Mercury. The vertical dashed line marks the arrival time of the CME-driven shock at *MESSENGER*. The horizontal dotted line in the bottom panel indicates the altitude (4 Mercury radii) below which data are excluded.

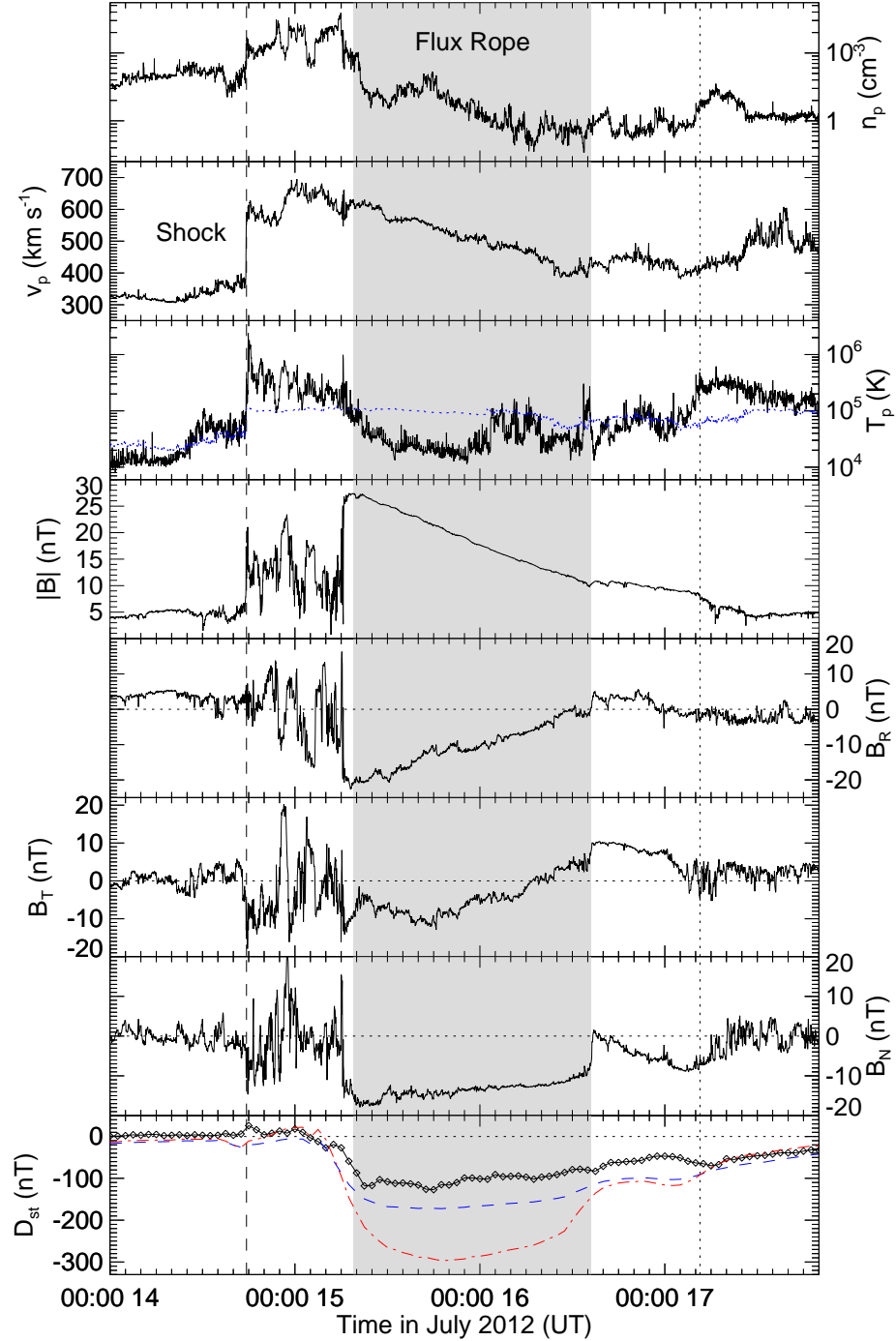


Figure 8. Solar wind plasma and magnetic field parameters associated with the 2012 July 12 CME observed at *Wind*. From top to bottom, the panels show the proton density, bulk speed, proton temperature, magnetic field strength and components, and D_{st} , respectively. The D_{st} profile is shifted 1 hour earlier for comparing with the *in situ* measurements. The dotted line in the third panel denotes the expected proton temperature calculated from the observed speed (Lopez 1987). The shaded region indicates the magnetic cloud interval determined by the GS reconstruction. The vertical dashed and dotted lines mark the arrival time of the shock and the end of the magnetic cloud, respectively. The blue dashed and red dot-dashed curves in the bottom panel represent D_{st} values estimated with the southward magnetic field component in GSM coordinates using the formulae of O’Brien & McPherron (2000) and Burton et al. (1975), respectively.

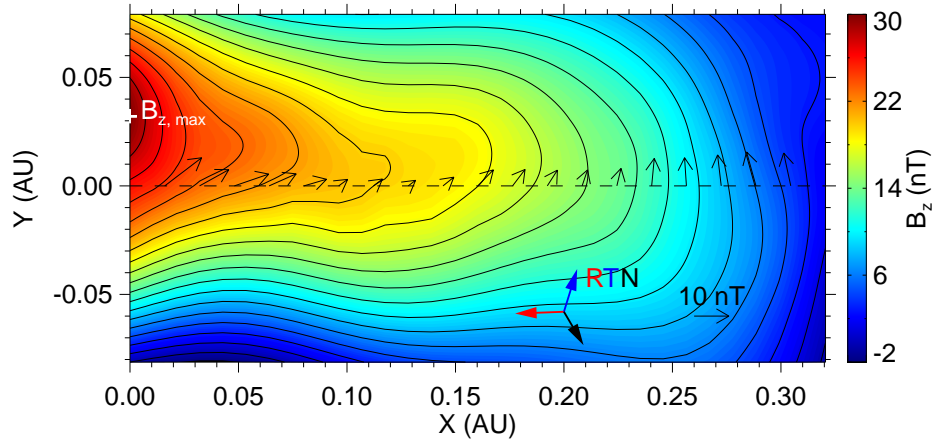


Figure 9. Reconstructed cross section of the magnetic cloud at *Wind*. Black contours show the distribution of the vector potential, and the color shading indicates the value of the axial magnetic field scaled by the color bar on the right. The location of the maximum axial field is indicated by the white cross. The dashed line marks the trajectory of *Wind*. The thin black arrows denote the direction and magnitude of the observed magnetic fields projected onto the cross section, and the thick colored arrows show the projected RTN directions.

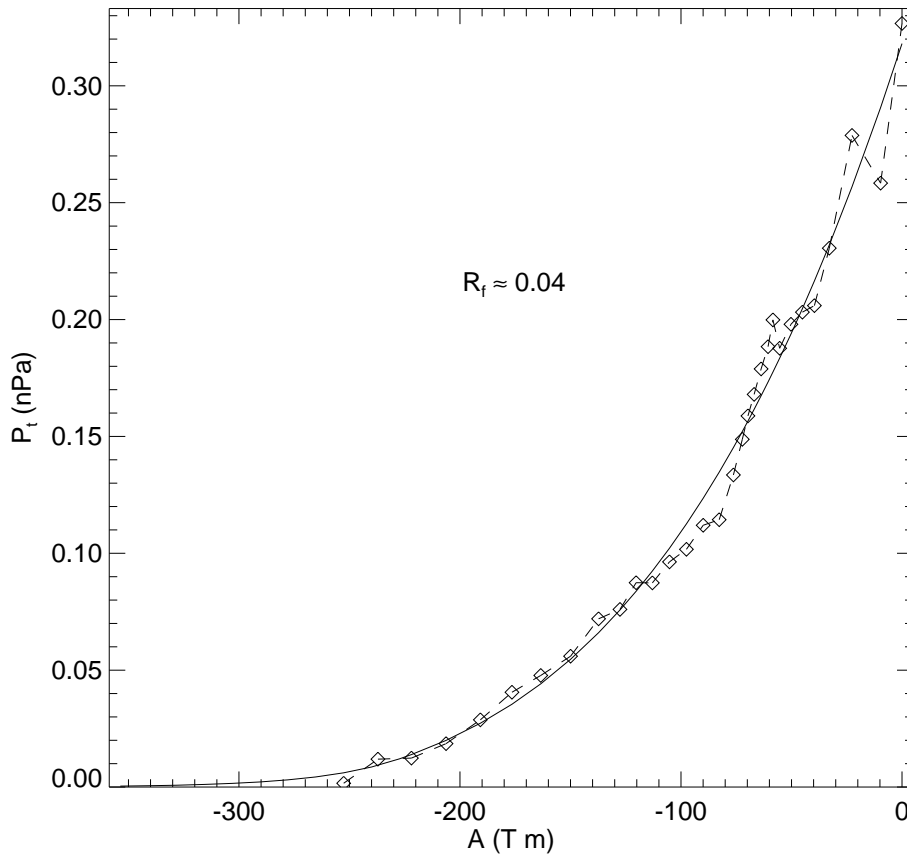


Figure 10. Transverse pressure P_t versus the vector potential A along the trajectory of *Wind*. The diamonds indicate measurements at *Wind*, and the solid curve is a fitted cubic polynomial combined with an exponential tail. The fitting residue R_f is defined by [Hu et al. \(2004\)](#).

REFERENCES

- Anderson, B. J., Acuña, M. H., Lohr, D. A., et al. 2007, *SSRv*, 131, 417
- Bougeret, J.-L., King, J. H., & Schwenn, R. 1984, *SoPh*, 90, 401
- Bougeret, J. L., Goetz, K., Kaiser, M. L., et al. 2008, *SSRv*, 136, 487
- Burton, R. K., McPherron, R. L., & Russell, C. T. 1975, *JGR*, 80, 4204
- Cheng, X., Ding, M. D., Zhang, J., et al. 2014, *ApJ*, 789, 93
- Cho, K.-S., Lee, J., Moon, Y.-J., et al. 2007, *A&A*, 461, 1121
- Claßen, H. T., & Aurass, H. 2002, *A&A*, 384, 1098
- Cremades, H., Iglesias, F. A., St. Cyr, O. C., et al. 2015, *SoPh*, 290, 2455
- Davies, J. A., Perry, C. H., Trines, R. M. G. M., et al. 2013, *ApJ*, 777, 167
- Davies, J. A., Harrison, R. A., Rouillard, A. P., et al. 2009, *GeoRL*, 36, 2102
- Dudík, J., Janvier, M., Aulanier, G., et al. 2014, *ApJ*, 784, 144
- Fainberg, J., & Stone, R. G. 1971, *SoPh*, 17, 392
- Farrugia, C. J., Jordanova, V. K., Thomsen, M. F., et al. 2006, *JGRA*, 111, A11104
- Feng, S. W., Chen, Y., Kong, X. L., et al. 2012, *ApJ*, 753, 21
- Good, S. W., & Forsyth, R. J. 2016, *SoPh*, 291, 239
- Good, S. W., Forsyth, R. J., Raines, J. M., et al. 2015, *ApJ*, 807, 177
- Gopalswamy, N., Lara, A., Lepping, R. P., et al. 2000, *GeoRL*, 27, 145
- Gopalswamy, N., Lara, A., Yashiro, S., Kaiser, M. L., & Howard, R. A. 2001a, *JGR*, 106, 29207
- Gopalswamy, N., Mäkelä, P., Xie, H., Akiyama, S., & Yashiro, S. 2009, *JGRA*, 114, A00A22
- Gopalswamy, N., Yashiro, S., Kaiser, M. L., Howard, R. A., & Bougeret, J.-L. 2001b, *ApJL*, 548, L91
- Harrison, R. A., Davies, J. A., Möstl, C., et al. 2012, *ApJ*, 750, 45
- Hau, L.-N., & Sonnerup, B. U. Ö. 1999, *JGR*, 104, 6899
- Hess, P., & Zhang, J. 2014, *ApJ*, 792, 49
- Howard, R. A., Moses, J. D., Vourlidas, A., et al. 2008, *SSRv*, 136, 67
- Hu, Q., Smith, C. W., Ness, N. F., & Skoug, R. M. 2004, *JGRA*, 109, 3102
- Hu, Q., & Sonnerup, B. U. Ö. 2002, *JGRA*, 107, 1142
- Kahler, S. W., & Webb, D. F. 2007, *JGRA*, 112, 9103
- Kaiser, M. L., Kucera, T. A., Davila, J. M., et al. 2008, *SSRv*, 136, 5
- Knock, S. A., Cairns, I. H., & Robinson, P. A. 2003, *JGRA*, 108, 1361
- Lavraud, B., Thomsen, M. F., Borovsky, J. E., Denton, M. H., & Pulkkinen, T. I. 2006, *JGRA*, 111, A09208
- Leblanc, Y., Dulk, G. A., & Bougeret, J.-L. 1998, *SoPh*, 183, 165
- Lemen, J. R., Title, A. M., Akin, D. J., et al. 2012, *SoPh*, 275, 17
- Liewer, P., Panasenco, O., Vourlidas, A., & Colaninno, R. 2015, *SoPh*, 290, 3343
- Lindsay, G. M., Luhmann, J. G., Russell, C. T., & Gosling, J. T. 1999, *JGR*, 104, 12515
- Liu, Y., Davies, J. A., Luhmann, J. G., et al. 2010a, *ApJL*, 710, L82
- Liu, Y., Luhmann, J. G., Huttunen, K. E. J., et al. 2008a, *ApJL*, 677, L133
- Liu, Y., Thernisien, A., Luhmann, J. G., et al. 2010b, *ApJ*, 722, 1762
- Liu, Y., Luhmann, J. G., Müller-Mellin, R., et al. 2008b, *ApJ*, 689, 563
- Liu, Y. D., Hu, H., Wang, C., et al. 2016, *ApJS*, 222, 23
- Liu, Y. D., Hu, H., Wang, R., et al. 2015, *ApJL*, 809, L34
- Liu, Y. D., Luhmann, J. G., Lugaz, N., et al. 2013, *ApJ*, 769, 45
- Liu, Y. D., Luhmann, J. G., Möstl, C., et al. 2012, *ApJL*, 746, L15
- Liu, Y. D., Luhmann, J. G., Kajdič, P., et al. 2014, *NatCo*, 5, 3481
- Lopez, R. E. 1987, *JGR*, 92, 11189
- Lugaz, N., Hernandez-Charpak, J. N., Roussev, I. I., et al. 2010, *ApJ*, 715, 493
- Lugaz, N., Vourlidas, A., & Roussev, I. I. 2009, *AnGeo*, 27, 3479
- Martínez-Oliveros, J. C., Raftery, C., Bain, H., et al. 2015, *SoPh*, 290, 891
- Marubashi, K., Akiyama, S., Yashiro, S., et al. 2015, *SoPh*, 290, 1371
- Möstl, C., Farrugia, C. J., Miklenic, C., et al. 2009, *JGRA*, 114, 4102
- Möstl, C., Temmer, M., Rollett, T., et al. 2010, *GeoRL*, 37, 24103
- Möstl, C., Farrugia, C. J., Kilpua, E. K. J., et al. 2012, *ApJ*, 758, 10
- Möstl, C., Amla, K., Hall, J. R., et al. 2014, *ApJ*, 787, 119
- Möstl, C., Rollett, T., Frahm, R. A., et al. 2015, *NatCo*, 6, 7135
- O'Brien, T. P., & McPherron, R. L. 2000, *JGR*, 105, 7707
- Pevtsov, A. A., Canfield, R. C., & Metcalf, T. R. 1995, *ApJL*, 440, L109
- Reiner, M. J., Kaiser, M. L., & Bougeret, J.-L. 2007, *ApJ*, 663, 1369
- Reiner, M. J., Kaiser, M. L., Fainberg, J., Bougeret, J.-L., & Stone, R. G. 1998, *GeoRL*, 25, 2493
- Reiner, M. J., Vourlidas, A., Cyr, O. C. S., et al. 2003, *ApJ*, 590, 533
- Rouillard, A. P., Lavraud, B., Sheeley, N. R., et al. 2010, *ApJ*, 719, 1385
- Saito, K., Poland, A. I., & Munro, R. H. 1977, *SoPh*, 55, 121
- Schou, J., Scherrer, P. H., Bush, R. I., et al. 2012, *SoPh*, 275, 229
- Sheeley, N. R., Walters, J. H., Wang, Y.-M., & Howard, R. A. 1999, *JGR*, 104, 24739
- Sheeley, Jr., N. R., Herbst, A. D., Palatchi, C. A., et al. 2008, *ApJ*, 675, 853
- Shen, F., Shen, C., Zhang, J., et al. 2014, *JGRA*, 119, 7128
- Solomon, S. C., McNutt, R. L., Gold, R. E., et al. 2001, *P&SS*, 49, 1445
- Song, H. Q., Chen, Y., Zhang, J., et al. 2015, *ApJL*, 808, L15
- Temmer, M., Vršnak, B., Rollett, T., et al. 2012, *ApJ*, 749, 57
- Thernisien, A. F. R., Howard, R. A., & Vourlidas, A. 2006, *ApJ*, 652, 763
- Vourlidas, A., Colaninno, R., Nieves-Chinchilla, T., & Stenborg, G. 2011, *ApJL*, 733, L23
- Wang, R., Liu, Y. D., Dai, X., et al. 2015, *ApJ*, 814, 80
- Wang, R., Liu, Y. D., Wiegmann, T., et al. 2016, *SoPh*, 291, 1159
- Wang, Y., Shen, C., Wang, S., & Ye, P. 2004, *SoPh*, 222, 329
- Winslow, R. M., Lugaz, N., Philpott, L. C., et al. 2015, *JGRA*, 120, 6101
- Wood, B. E., Howard, R. A., Plunkett, S. P., & Socker, D. G. 2009, *ApJ*, 694, 707
- Yurchyshyn, V. B., Wang, H., Goode, P. R., & Deng, Y. 2001, *ApJ*, 563, 381